Research Article

The synergistic effects study between metal oxides and graphene on far-infrared emission performance

Xiaomin Zhao[1] · Yihong Zhang[1] · Jianfeng Xu[1] · Danqing Chen[1] · Guohua Chen[1]

Abstract

Materials with high far-infrared (FIR) emissivity are quiet promising in modern medical care field, owing to its accelerating effects to blood circulation and metabolism. In this work, we synthesized two serials composites: MnO_2/graphene nanoplate (GNPs) and Fe_2O_3/GNPs via in situ hydrothermal process. Positive synergistic effects on FIR emission were shown between either MnO_2 or Fe_2O_3 and GNPs. In particular, MnO_2/GNPs (2%) showed a super high FIR emissivity of 0.981 compared with pristine MnO_2 (0.940) and GNPs (0.878) in the wavelength of 8–14 μm. The FIR emissivity of Fe_2O_3/GNPs (1%) was up to 0.953 that was much higher than those of pristine Fe_2O_3 (0.877) and GNPs as well. Benefiting from the characteristics of graphene such as large specific surface, lightweight and thin-layer, MnO_2 and Fe_2O_3 nanocrystals grew on graphene surface and formed different morphologies. A coralloid-like morphology was formed to MnO_2/GNPs (2%), suggesting a highly porous surface that meant more unstable atoms or molecules were exposed. The morphologies of metal oxide/GNPs were thought to relate with the good synergistic effects between GNPs and metal oxides. Therefore, this work provides that metal oxides/graphene composites have promising application for high FIR emission materials.

Keywords Graphene · MnO_2 · Fe_2O_3 · Far-infrared emission

1 Introduction

Since the heightened awareness of human healthy, materials with FIR emission are quite popular in medical care products including warm-up cloth, bedding, footare, knee-cap and waistband, owing to that human body is easy to absorb FIR ray with wavelength 8–14 μm that can accelerate the blood circulation and metabolism [1–3]. Hence, materials with high FIR emissivity are in great demand nowadays. Graphene and its derivatives have attracted numerous attention for advanced materials due to the unique thermal and electrical conductivity, high mechanical strength and optical properties [4–10]. However, the research on the FIR absorbing and emitting capability of graphene is rarely studied. Hu et al. coated graphene nanoplate on cotton fabric by using polyurethane as adhesive [11]. The FIR emissivity of cotton increased from 0.867 to 0.911 after finishing, showing a novel potential application to FIR emission material for graphene. Traditionally, metal oxides from the III ~ V periodic elements show good FIR emissivity, such as Al_2O_3 [12], MgO [12, 13], TiO_2 [14, 15], SiO_2, Cr_2O_3 [16], ZrO_2 [17], MnO_2 [18], Fe_2O_3 [19] and ZrC [20]. The current FIR emission materials are mainly prepared through blending or coating these metal oxides directly into matrix. Shim et al. simply blended ceramic compounds (MU-4 N and RT-3, complex of SiO_2, Fe_2O_3, Al_2O_3, CaO and Na_2O) to hydrophilic polyurethane films to form film laminate textiles [21]. With a 20 wt.% loading, the FIR emissivity of prepared textile was 0.89. Although FIR emissivity increased, the high loading of inorganic

---

particle would influence the mechanical properties. Above all, graphene is a novel promising candidate for high FIR emission material compared with traditional FIR emission additives. To develop graphene composites with high FIR emissivity is meaningful for modern medical care technologies. Herein, we prepared composites of graphene and metal oxides (MnO_2, Fe_2O_3) with high FIR emissivity via hydrothermal process in this work. The impact of GNP content on FIR emissivity of metal oxide was studied. With a 2 wt.% loading of GNPs, the FIR emissivity of MnO_2 raised from 0.94 to 0.981 and that of Fe_2O_3 with 1 wt.% GNPs raised from 0.877 to 0.953. The results revealed apparent synergistic effect between GNPs/MnO_2 (or Fe_2O_3). In present of GNPs, MnO_2 and Fe_2O_3 crystals grew on graphene surface with a different way compared with themselves. A coralloid-like morphology was formed to the MnO_2 with a 2 wt.% loading of graphene, suggesting a highly porous MnO_2/graphene composites. By measuring the BET nitrogen absorption and desorption curve, it was clear that GNPs addition increased the specific surface area and the pore volume. Hence, the morphologies of metal oxide/GNPs were thought to relate with the good synergistic effects between GNPs and metal oxides.

2 Experimental

2.1 Material

GNPs (KNG-G5) was supplied by Xiamen Knano Graphene Technology Co., Ltd. $KMnO_4$ was purchased from Xilong Scientific Co., Ltd. H_2SO_4, H_2O_2, and $FeCl_3{\cdot}6H_2O$ were purchased from Sinopharm Chemical Reagent Co., Ltd.

2.2 The preparation of GNPs/MnO_2 composite

GNPs/MnO_2 composites were synthesized via the redox reaction between GNPs and $KMnO_4$ under hydrothermal process. Briefly, GNPs (0.2 g) was dispersed in 100 mL deionized water via ultrasonic vibration for 1 h. A certain amount of $KMnO_4$ was solved in the GNPs dispersion. Subsequently, the final mixture suspension was reacted in a 150 mL hydrothermal reactor under 150 °C for 6 h. Then the reactor was opened after cooling down naturally. The raw solid product was filtered and washed by deionized water for three times. The obtained GNPs/MnO_2 composites was dried under 80 °C for 1 day. For comparison, pure birnessite- type MnO_2 was also synthesized.

2.3 The preparation of GNPs/Fe_2O_3 composites

GNPs/Fe_2O_3 composites were synthesized via a similar hydrothermal process between GNPs and $FeCl_3$ with

that of GNPs/MnO_2 composites. The difference is that the temperature and duration of hydrothermal process were 200 °C and 10 h, respectively.

2.4 Characterization

The micro morphology of the as-prepared materials was observed by a field-emission scanning electron microscopy (SEM, NJSM-6700F, JEOL, Japan) and transmission electron microscope (TEM, JEOL-2100F, Japan). The crystallographic structures were determined by a powder XRD system (D8-Advance, Bruker, Germany) equipped with Cu Kα radiation (λ = 0.15406 nm) with a scan rate (2θ) of 5°/min and an accelerating voltage of 40 kV. The Raman spectra were recorded from 500 to 3500 cm^{-1} on a Raman spectrometer (Raman, LABRAM, HJY, France) equipped with a 532 nm wavelength laser. FIR emissivity was measured by dual-band emissivity meter (IR-2, Shanghai Chengbo Optoelectronic Technology, China) with a range of 8–14 μm. The specific surface area, pore volume and pore size was measured by the Brunauer–Emmett–Teller (BET) method via nitrogen adsorption–desorption measurements at a liquid nitrogen temperature using a NOVA 2000e analyzer (Quantachrome, USA).

3 Results and discussion

Scheme 1 illustrated the hydrothermal procedure to fabricate the MnO_2/GNPs and Fe_2O_3/GNPs composites. Firstly, GNPs (0.2 g) was dispersed in 100 mL deionized water under ultrasonic vibration for 1 h. A certain amount of $KMnO_4$ was then solved in the GNPs dispersion. MnO_2 crystals formed and grew on GNPs surface via the redox reaction between GNPs and $KMnO_4$, when the final mixture suspension was reacted in a 150 mL hydrothermal reactor at 150 °C for 6 h. Fe_2O_3/GNPs composites were synthesized via the redox reaction between GNPs and $FeCl_3$ under a similar hydrothermal process with that of MnO_2/GNPs composites. The difference is that the temperature and duration of hydrothermal process were 200 °C and 10 h, respectively. Table 1 listed the self-prepared MnO_2/GNPs and Fe_2O_3/GNPs composites at various loading of GNPs.

The morphology of MnO_2, MnO_2/GNPs, Fe_2O_3 and Fe_2O_3/GNPs composites were observed by SEM and TEM. Seen in Fig. 1a, MnO_2 prepared via the hydrothermal process presented a spherical flower structure formed by many nanoflakes. Its diameter ranged from 2 to 4 μm. The large specific surface area of GNPs enabled metal oxide easily grown on GNPs via hydrothermal process. In Fig. 1b, it is notable that MnO_2/GNPs showed a highly porous surface with uniformly diameter, indicating that a layer of MnO_2

Scheme 1 The hydrothermal process of MnO$_2$/GNPs and Fe$_2$O$_3$/GNPs composites
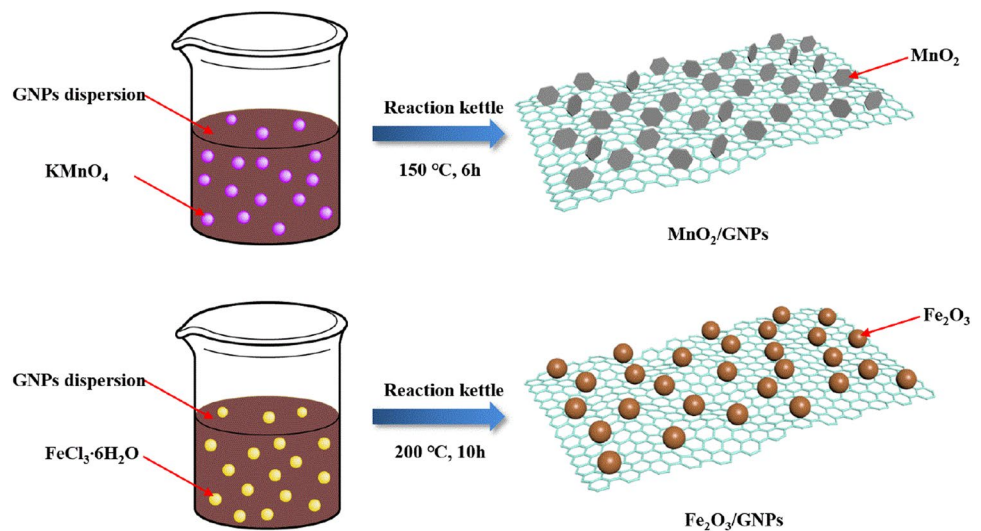
Table 1 All the samples and their FIR emissivity

Sample	GNPs content (wt.%)	FIR emissivity
GNPs	100	0.878
MnO$_2$/GNPs-20	20	0.940
MnO$_2$/GNPs-10	10	0.964
MnO$_2$/GNPs-5	5	0.975
MnO$_2$/GNPs-2	2	0.981
MnO$_2$	0	0.940
Fe$_2$O$_3$/GNPs-10	10	0.869
Fe$_2$O$_3$/GNPs-5	5	0.909
Fe$_2$O$_3$/GNPs-3	3	0.910
Fe$_2$O$_3$/GNPs-1	1	0.953
Fe$_2$O$_3$	0	0.877

Fig. 1 SEM images of MnO$_2$ (**a**), MnO$_2$/GNPs (**b**) and TEM images of MnO$_2$/GNPs (**c** and **d**)

particles covered GNPs uniformly during the hydrothermal process. As shown in Fig. 1b, a coralloid-like morphology was shown due to the resembling of highly porous MnO$_2$ on the surface of GNPs. Figure 1c, d showed the TEM images of MnO$_2$/GNPs nanocomposite at different magnifications, respectively. The numerous tiny nanoflakes of MnO$_2$ connected with each other and uniformly dispersed on the surface of GNPs (Fig. 1c). Compared with the microsphere in Fig. 1a, the size of MnO$_2$ grown on GNPs was smaller than that of pristine MnO$_2$. In Fig. 1d, the interface between GNPs and MnO$_2$ layer was clearly shown. MnO$_2$ nanoflakes grew directly on the surface of GNPs, forming ordered aligned MnO$_2$ arrays, rather than deposited. The interplanar spacing of the nanoflakes was measured to be 0.704 nm, which was much close to the as-reported value for birnessite-type of MnO$_2$ [22, 23].

The porous MnO$_2$ structure was reported to easily form via a hydrothermal process of KMnO$_4$ solution [24]. The formation of MnO$_2$ was from the decomposition of KMnO$_4$, which was expressed as:

$$4MnO_4^- + 3C + H_2O \rightarrow 4MnO_2 + CO_3^{2-} + 2HCO_3^-$$
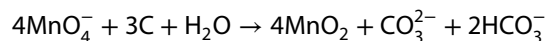
In present of GNPs, the decomposition rate of KMnO$_4$ might be accelerated owing to a possible catalytic effect of GNPs. Under hydrothermal process, the self-assembling rate of MnO$_2$ nanocystallines could not catch up the production rate. The MnO$_2$ nanocystallines initially grown on GNPs then acted as the new nucleation sites, resulting that the nanoflakes was formed along with the surface of GNPs. Therefore, a highly porous MnO$_2$ layer covered on the surface of GNPs and the size of MnO$_2$ particles was smaller than that of pristine MnO$_2$.

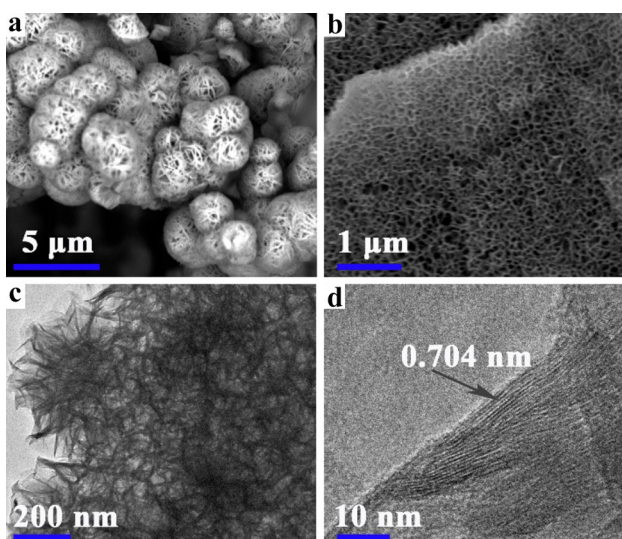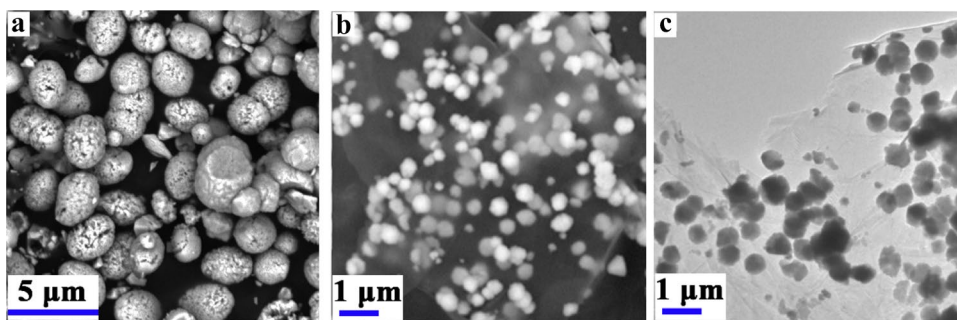In Fig. 2a, pristine Fe$_2$O$_3$ synthesized via the hydrothermal process showed an elliptic spherical structure along

Fig. 2 SEM images of Fe_2O_3 (**a**), GNPs/Fe_2O_3 (**b**) and TEM images of GNPs/Fe_2O_3 (**c**)

with a path length ranged from 0.8 to 2.5 μm. In present of GNPs, Fe_2O_3 particles grew on the surface of GNPs and their sizes were smaller than 0.5 μm, as shown in Fig. 2b. The TEM image of GNPs/Fe_2O_3 (Fig. 2c) showed that Fe_2O_3 particles were solid spheres, rather than hollow ones. Notably, Fe_2O_3 particles were loosely rather than connected with each other.

Figure 3a described the XRD patterns of GNPs and MnO_2/GNPs-2 at different loading of GNPs. The diffraction peaks at 26.4° on XRD pattern of GNPs was assigned to the (002) reflection of GNPs. This peak appeared due to the stacking of GNPs sheets. On XRD patterns of MnO_2/GNPs, the diffraction peak of GNPs was rather weak. On one side, GNPs loadings was only 2 wt.%. On another side, the coating of the MnO_2 layer was thick and intensely covered all over the GNPs sheet, which might decrease the intensity of (002) reflection peak of GNPs. The diffraction 2θ peaks at 21.2°, 26.9°, 35.6° and 65.6° were assigned to the birnessite-type MnO_2 (JCPDS number 80-1098) composed of 2D edge-shared MnO_6 octahedral layers with K^+ cations and H_2O molecules in the interlayer space. The two peaks at 21.2° and 26.9° were related with the (001) and (002) basal reflections, respectively, while the two peaks at 35.6° and 65.6°

were related with (20 l/11 l) and (02 l/31 l) diffraction, respectively. The XRD patterns of Fe_2O_3 synthesized by the hydrothermal process was assigned to the hematite α-Fe_2O_3 (JCPDS number 33-0664). The 2θ peaks at 24.2°, 33.2°, 35.6°, 40.9°, 49.6°, 54.1°, 57.6°, 62.5° and 64.0° were related with the (012), (104), (110), (113), (024), (116), (122), (214) and (300) basal reflections, respectively. On XRD pattern of Fe_2O_3/GNPs-1 (Fig. 3b), the reflection of GNPs was still visible at 26.4° since spherical Fe_2O_3 was dispersedly grown on GNPs rather than with a manner of intensely porous coating as like the MnO_2.

The Raman spectra further confirmed the structure feature of GNPs, MnO_2/GNPs and Fe_2O_3/GNPs. In Fig. 4, pristine GNPs showed three characteristic peaks at 1350 (D band) and 1575 cm^{-1} (G band), respectively. Along with the growth of MnO_2, the three peaks showed at the same positions on Raman spectrum of MnO_2/GNPs. The birnessite-type MnO_2 showed three characteristic peaks located at 500, 575, and 651 cm^{-1}, respectively, which was in agreement with the reported data [25]. α-Fe_2O_3 showed feature peaks at 222, 290, 405, 606 and 1300 cm^{-1} [26]. On Raman spectrum of Fe_2O_3/GNPs, the peak at 1300 cm^{-1} was overlapped with the D-band of GNPs as one broad peak. Above all, the results of Raman test were accordance
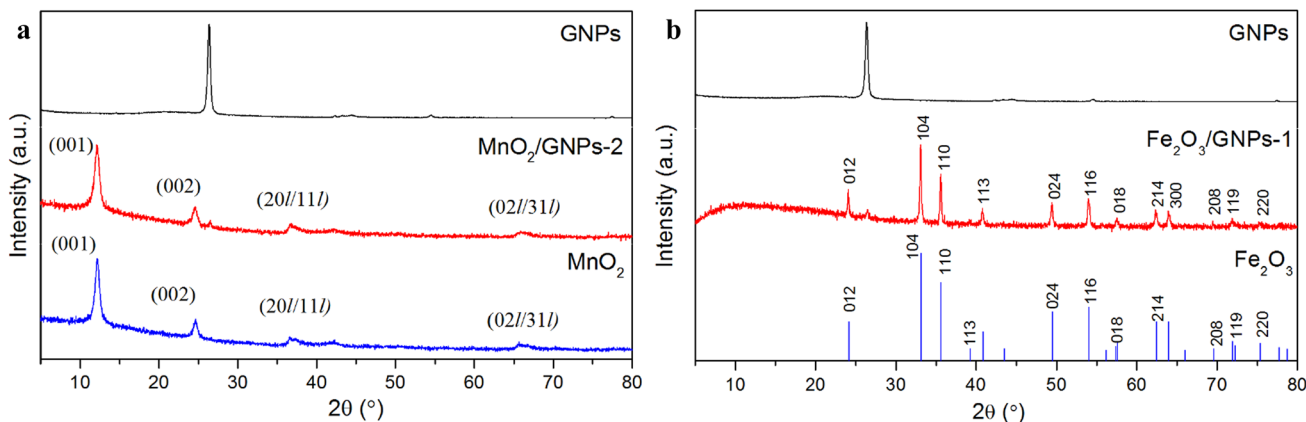

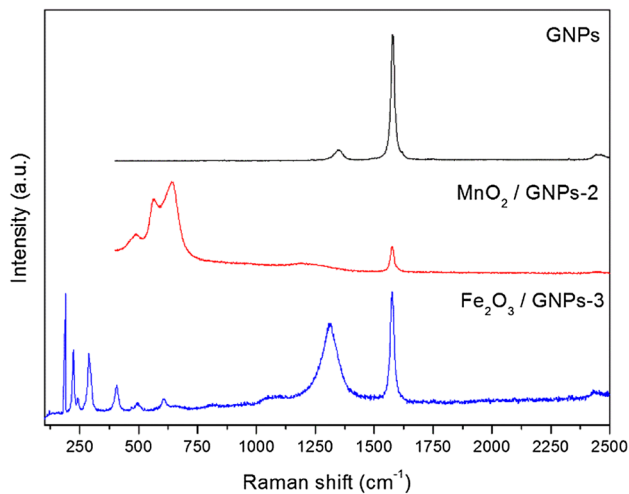**Fig. 3** The XRD curves of GNPs, MnO_2, MnO_2/GNPs, Fe_2O_3 and Fe_2O_3/GNPs

Fig. 4 Raman spectra of GNPs, MnO₂/GNPs and Fe2O3/GNPs

with those of XRD. The synthesis of MnO₂/GNPs and Fe₂O₃/GNPs were successful.

The FIR emission performances were measured with a wavelength range from 8 to 14 μm. The emissivity (ε) is defined as the ratio of radiant emittance of an object to that of a blackbody. Generally, ε of one material drops in the range of $0 < ε < 1$.

A good FIR emission material has ε close to 1. Figure 5a, b described the variation of ε of MnO₂/GNPs and Fe₂O₃/GNPs with different loadings of GNPs. To show the synergistic effect of GNPs and metal oxide (MO), the calculated (*Cal.*) ε of GNPs/MO was calculated as following equation:

$$Cal.\varepsilon = \varepsilon_{GNPs} \times w_{GNPs} + \varepsilon_{MO} \times w_{MO}$$

ε of pristine MnO₂ and GNPs were 0.940 and 0.878, respectively. In Fig. 5a, Cal. ε of MnO₂/GNPs was linearly reduced

and the value ranged in the above two limit ε values as the GNPs loadings raised. Although the experimental (*Exp.*) ε followed the similar trend, the value was much higher than the *Cal.* ε of MnO₂/GNPs. The *Exp.* ε of MnO₂/GNPs (2%) reached up to 0.981 which was higher than 0.940 of pristine MnO₂. The results presented a positive synergistic effect existed between GNPs and MnO₂. This phenomenon existed in Fe₂O₃/GNPs system as well. Pristine Fe₂O₃ had almost equal ε (0.877) with GNPs. *Cal.* ε of each Fe₂O₃/GNPs (1, 3, 5 and 10%) were all close to 0.878. However, *Exp.* ε of Fe₂O₃/GNPs (1, 3, 5 and 10%) were 0.953, 0.910, 0.909 and 0.869, respectively. When GNPs loadings were 1, 3 and 5%, the synergetic effect between GNPs and Fe₂O₃ greatly improved the FIR emission performance of pristine GNPs and Fe₂O₃ (Fig. 5b). Therefore, the FIR ray emission of MnO₂ and Fe₂O₃ were improved owing to the addition of GNPs.

Table 2 collected the data of specific surface area (SA), pore volume and pore diameter of pristine MnO₂ and MnO₂/GNPs (2%). The average pore diameter of MnO₂/GNPs (2%) was 3.8 nm as well as the pore size of pristine MnO₂. It was reasonable that GNPs afforded the surface for MnO₂ microcrystalline to align its structure, while it did not change the pore forming style. The large specific surface of GNPs increased the SA of MnO₂ from 40.2 to 50.7 m³/g. The pore volume increased from 0.04 to 0.32 mL/g as well, resulting from the more porous structure of MnO₂/GNPs. It was considered that the enlarged specific surface

Table 2 The specific surface area, pore volume and pore diameter of pure MnO₂ and MnO₂/GNPs

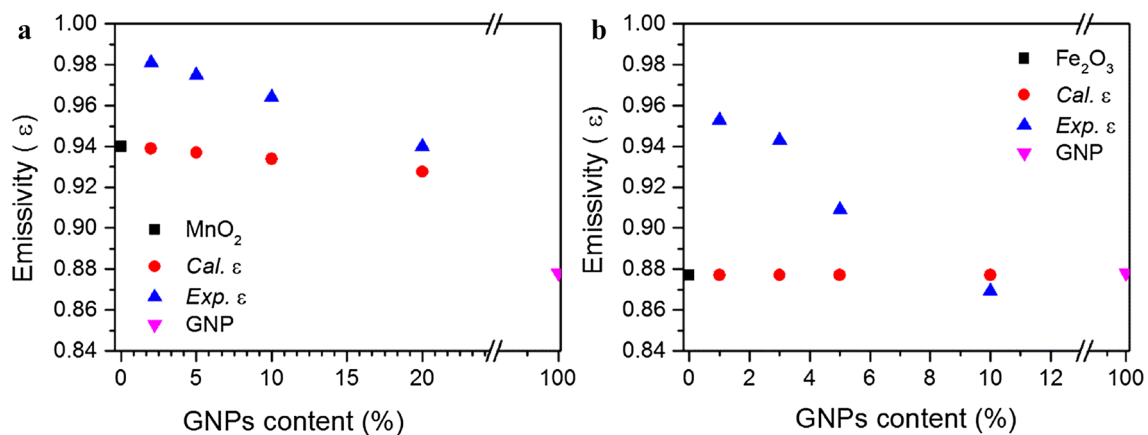| Sample	SA(m³/g)	Pore volume (mL/g)	Average pore diameter (nm)
MnO₂	40.2	0.04	3.8
MnO₂/GNPs	50.7	0.32	3.8

Fig. 5 The FIR emissivity of MnO₂/GNPs (**a**) and Fe₂O₃/GNPs (**b**)

brought about the increase of surface energy, owing to the increase of exposed molecule number on the surface. Herein, MnO_2/GNPs had larger SA than that of pristine MnO_2, indicating that more unstable atoms or molecules were exposed, resulting to a high FIR emissivity of MnO_2/GNPs. This is a preliminary judgment for the positive synergistic effect between MnO_2 and GNPs, while it was poor to explain the mechanism for the Fe_2O_3/GNPs system.

4 Conclusion

In summary, metal oxides (MnO_2 and Fe_2O_3)/GNPs composites were synthesized by in situ hydrothermal process. Both MnO_2/GNPs and Fe_2O_3/GNPs showed positive synergistic effect on FIR emission. MnO_2/GNPs(2%) showed a higher FIR emissivity of 0.981 compared with pristine MnO_2 and GNPs. The coralloid-like morphology of MnO_2/GNPs played important role on increasing FIR emissivity due to the enlarged specific surface area and pore volume. The FIR emissivity of Fe_2O_3/GNPs (1%) was up to 0.953 that was much higher than those of pristine Fe_2O_3 and GNPs, while the synergistic effect between Fe_2O_3 and GNPs needed to be studied in future. According to the FIR emissivity of current market products (> 0.8), this work shows that metal oxides/graphene composites is one promising choice for the high FIR emission materials in medical care application.

Compliance with ethical standards

Conflicts of interest The authors declare that they have no conflict of interst.

References

1. Fitzgerald AJ, Berry E, Zinovev NN, Walker GC, Smith MA, Chamberlain JM (2002) An introduction to medical imaging with coherent terahertz frequency radiation. Phys Med Biol 47(7):R67
2. Ise N, Katsuura T, Kikuchi Y, Miwa E (1987) Effect of far-infrared radiation on forearm skin blood flow. Ann Physiol Anthropol 6(1):31–32
3. Toyokawa H, Matsui YJ, Tsuchiya H, Teshima S, Nakanishi H, Kwon AH, Azuma Y, Nagaoka T, Ogawa T, Kamiyama Y (2003) Promotive effects of far-infrared ray on full-thickness skin wound healing in rats. Exp Biol Med 228(6):724–729
4. Bonaccorso F, Colombo L, Yu G, Stoller M, Tozzini V, Ferrari AC, Ruoff RS, Pellegrini V (2015) 2D materials. Graphene, related two-dimensional crystals, and hybrid systems for energy conversion and storage. Science 347(6217):1246501
5. Kim H, Abdala AA, Macosko CW (2015) Graphene/Polymer nanocomposites. Macromolecules 43(16):6515–6530
6. Li Z, Guo Q, Li Z, Fan G, Xiong DB, Su Y, Zhang J, Zhang D (2015) Enhanced mechanical properties of graphene (reduced graphene oxide)/aluminum composites with a bioinspired nanolaminated structure. Nano Lett 15(12):8077–8083
7. Raccichini R, Varzi A, Passerini S, Scrosati B (2015) The role of graphene for electrochemical energy storage. Nat Mater 14(3):271–279
8. Wang X, Huang Y, Jia D, Wei KP, Guo Z, Du Y, Tang X, Cao Y (2015) Self-assembled sandwich-like vanadium oxide/graphene mesoporous composite as high-capacity anode material for lithium ion batteries. Inorg Chem 54(24):11799–11806
9. Xiao-Xiong HU, Jiang GD, Wei M, Yuan SD (2015) The preparation of graphene/TiO_2 composites with enhanced photocatalytic activity. J Wuhan Univ Technol 37(2):11–17
10. Zheng XT, Ananthanarayanan A, Luo KQ, Chen P (2015) Glowing graphene quantum dots and carbon dots: properties, syntheses, and biological applications. Small 11(14):1620–1636
11. Hu X, Tian M, Qu L, Zhu S, Han G (2015) Multifunctional cotton fabrics with graphene/polyurethane coatings with far-infrared emission, electrical conductivity, and ultraviolet-blocking properties. Carbon 95:625–633
12. Billard D, Gervais F, Piriou B (1980) Farinfrared absorption in Al_2O_3 and MgO. Int J Infrared Millimeter Waves 1(4):641–647
13. Guo HC, Liu WM, Tang SH (2007) Terahertz time-domain studies of far-infrared dielectric response in 5 mol% MgO:LiNbO$_3$ ferroelectric single crystal. J Appl Phys 102(3):1784
14. Murray DB, Netting CH, Saviot L, Pighini C, Millot N, Aymes D, Liu HL (2006) Far infrared absorption by acoustic phonons in titanium dioxide nanopowders. J Nanoelectron Optoelectron 1(1):92–98
15. Song X (2007) Study on TiO_2-mullite far-infrared ceramic. Rare Metal Mater Eng 36:471–473
16. Adam C, Vogel C, Lipiec E, Stemann J, Holldack K, Sekine R (2015) Thermal treatment of chromium(III) oxide with carbonates analyzed by far-infrared spectroscopy. Appl Spectrosc 69(10):1210
17. Chen TY, Cho HP, Jwo CS, Hung MH, Lee WS (2015) Analyzing how the ZrO_2 far infrared material affects the performance of smooth tube heat exchangers. J Nanomater 1:118
18. Xue G, Wang YQ, Zhang L, Zhang XF (2010) Preparation of tourmaline composite materials and its property of far infrared radiance. Adv Mater Res 96:165–170
19. Liu J, Meng J, Liang J, Huo X (2014) Effect of far infrared radiation ceramics containing rare earth additives on surface tension of water. J Rare Earths 9:890–894
20. Xu J, Jiang S, Wang Y, Shang S, Miao D, Guo R (2017) Photothermal conversion and thermal insulation properties of ZrC coated polyester fabric. Fibers Polym 18(10):1938–1944
21. Park CH, Shim MH, Shim HS (2006) Far IR emission and thermal properties of ceramics coated fabrics by IR thermography. Key Eng Mater 321–323:849–852
22. Liu Z, Ma R, Ebina Y, Takada K, Sasaki T (2007) Synthesis and delamination of layered manganese oxide nanobelts. Chem Mater 19(26):6504–6512
23. Zhu HT, Luo J, Yang HX, Liang JK, Rao GH, Li JB, Du ZM (2008) Birnessite-type MnO_2 nanowalls and their magnetic properties. J Phys Chem C 112(44):17089–17094
24. Xia H, Wang Y, Lin J, Lu L (2012) Hydrothermal synthesis of MnO_2/CNT nanocomposite with a CNT core/porous MnO_2 sheath hierarchy architecture for supercapacitors. Nanoscale Res Lett 7(1):33
25. Ogata A, Komaba S, Baddour-Hadjean R, Pereira-Ramos JP, Kumagai N (2008) Doping effects on structure and electrode

performance of k-birnessite-type manganese dioxides for rechargeable lithium battery. Electrochim Acta 53(7):3084–3093

26. Reddy MV, Yu T, Sow CH, Shen ZX, Lim CT, Subba Rao GV, Chowdari BVR (2007) α-Fe2O3 Nanoflakes as an Anode Material for Li-Ion Batteries. Adv Func Mater 17(15):2792–2799